

On spinodal decomposition in alnico—a transmission electron microscopy and atom probe tomography study

Lin Zhou^{a,*}, Wei Guo^b, Jonathan D. Poplawsky^b, Liqin Ke^a, Wei Tang^a, Iver E. Anderson^a, Matthew J. Kramer^a

^aAmes Laboratory, U.S. Department of Energy, Ames, Iowa 50011, USA

^bCenter for Nanophase Materials Sciences, Oak Ridge National Laboratory, Oak Ridge, TN 37831, USA

Abstract

Alnico is a prime example of a finely tuned nanostructure whose magnetic properties are intimately connected to magnetic annealing (MA) during spinodal transformation and subsequent lower temperature annealing (draw) cycles. Using a combination of transmission electron microscopy and atom probe tomography, we show how these critical processing steps affect the local composition and nanostructure evolution with impact on magnetic properties. The nearly 2-fold increase of intrinsic coercivity (H_{ci}) during the draw cycle is not adequately explained by chemical refinement of the spinodal phases. Instead, increased Fe-Co phase (α_1) isolation, development of Cu-rich spheres/rods/blades and additional α_1 rod precipitation that occurs during the MA and draw, likely play a key role in H_{ci} enhancement. Chemical ordering of the Al-Ni-phase (α_2) and formation of Ni-rich (α_3) may also contribute. Unraveling of the subtle effect of these nano-scaled features is crucial to understanding on how to improve shape anisotropy in alnico magnets.

Keywords: Magnetic, Microstructure, Spinodal decomposition, Atom-probe tomography, TEM, STEM HAADF

1. Introduction

Using an external magnetic field during heat-treatment, magnetic annealing (MA), to control materials' microstructure has been widely studied since the 1950s [1]. MA promotes formation of texture, biases spinodally decomposed phase morphologies, promotes martensitic transformation in ferrous alloys, changes phase transformation temperatures, etc [2, 3]. Cahn showed that MA is most effective in alnico magnets at a temperature near the onset of spinodal decomposition (SD) and below the Curie temperature [4]. Alnico has recently re-attracted a large amount of interest as a near-term, non-rare-earth permanent magnetic alloy for wind power generators and electric vehicle motors [5–7]. Its lower cost and stable performance over a wide temperature range make it still irreplaceable after eighty years of development.

Unlike rare-earth based permanent magnets, coercivity in alnico is provided by shape anisotropy, instead of intrinsic magneto-crystalline anisotropy. As a result, magnetic properties of alnico strongly depend on the details of its unique microstructure: a periodically arrayed elongated Fe-Co rich (α_1) hard magnetic phase embedded in a continuous non-magnetic Ni-Al-rich (α_2) matrix, formed via SD. Achieving the optimum properties in alnico requires a well controlled and lengthy heat-treatment process, including solutionization of the alloy above 1200 °C, isothermal MA near its Curie temperature and subsequent lower temperature annealing (draw cycles) [1, 8–12]. The application of MA marks the most important cornerstone in alnico magnets' development history. MA biases the α_1 phase's

morphology during SD and make it grow along the $\langle 100 \rangle$ crystallographic direction closest to the external field [13]. The resulting anisotropic spinodal nano-structure has significantly improved coercivity (H_{ci}) and remanence (B_r) of alnico. The biased growth is optimal only when it is performed within a narrow temperature range for a limited time. For example, the ideal morphology (in transverse cross-section) that brings optimum H_{ci} in higher grade alnico 8 and 9 series is a mosaic structure consisting of periodically arrayed ~ 40 nm diameter α_1 phases embedded in a continuous α_2 matrix obtained by MA at ~ 840 °C [14].

On the other hand, the microstructure and chemistry changes during the lower temperature draw process are much more subtle, although draw cycles play an equally important role in increasing H_{ci} in alnico. For example, our recent study showed that for alnico 8H, its coercivity was nearly doubled after drawing, compared to the MA alone [14]. More interestingly, the absolute increase during the draw-related H_{ci} enhancement was almost independent of the preceding MA temperature. However, the mechanism behind H_{ci} enhancement during draw remains surprisingly elusive and is not well understood despite the fact that drawing has been practiced for decades. Most previous understanding on draw enhancement of H_{ci} was based on a simplistic assumption: lower temperature annealing results in a larger composition separation and a larger magnetization difference between α_1 and α_2 phases, which increases the H_{ci} [1]. This assumption appears oversimplified, especially considering the recent findings which reveal an insignificant compositional variation before and after the draw [14]. This lack of understanding is mainly due to our inability to access and evaluate the very subtle nature of chemical and microstructural evolution during the draw. Revealing these subtle effects appears crucial to

*Corresponding author

Email address: linzhou@ameslab.gov (Lin Zhou)

improve shape anisotropy in permanent magnets or reduce coercivity in soft magnetic alloys.

This study was designed to elucidate the structural and chemical evolution in alnico at different stages during heat treatment, especially during the draw process, as well as their relationship with magnetic properties. An isotropic (alnico 8H) 32.4Fe-38.1Co-12.9Ni-7.3Al-6.4Ti-3.0Cu (wt%) alloy was chosen for this investigation. A combination of electron backscatter diffraction (EBSD), atom probe tomography (APT), and transmission electron microscopy (TEM) techniques were used to better discover and more precisely characterize the morphology and chemistry in SD phases. Based on our comprehensive characterization results, we discuss H_{ci} enhancement mechanisms beyond the conventional explanation.

2. Experimental details

2.1. Sample preparation and property measurement

Batch of pre-alloyed powder was made by gas-atomization in Ames Laboratory. Details on magnet alloy consolidation to full density by hot isostatic pressing have been reported elsewhere [15]. The resultant alloy was polycrystalline with randomly oriented grains. Center sections of the alloy were cut into 3 mm diameter by 8 mm cylinders. The cylindrical samples were solutionized at 1250 °C for 30 min in vacuum and quenched in an oil bath (sample 1). Some samples were then annealed at 840 °C with an external applied field of 1 T for 0.5, 1.5, 5, and 10 min, with corresponding samples labeled as 2 thru 5, respectively. This MA temperature was determined from our previous study which gives optimum alloy magnetic properties [15]. Some samples also underwent an additional low temperature drawing process at 650 °C for 1, 3, and 5 h (labeled 6 thru 8), respectively. After MA or low temperature draw, the samples were water quenched to room-temperature. Details of heat-treatment conditions of samples 1–8 are listed in Table 1. Their magnetic properties were measured using a Laboratorio Elettrofisico Engineering Walker LDJ Scientific AMH-5 Hysteresis graph in a closed-loop setup.

Table 1: Detailed heat-treatment conditions for samples 1 to 8.

Samples	1	2	3	4	5	6	7	8
MA/840 °C (min)	0	0.5	1.5	5	10	10	10	10
Draw/650 °C (h)	0	0	0	0	0	1	3	5

2.2. Characterization

APT and TEM are sensitive methods for investigating details of structure and compositions of materials down to atomic-scale resolution [16, 17]. In this study, APT analysis of samples 1 to 8 was performed to better understand the SD phase morphology in three dimensions, as well as a more accurate determination of the α_1 and α_2 composition and morphology at different heat-treatment stages. TEM was used to reveal the crystallographic relationship between different phases. In each sample, grains

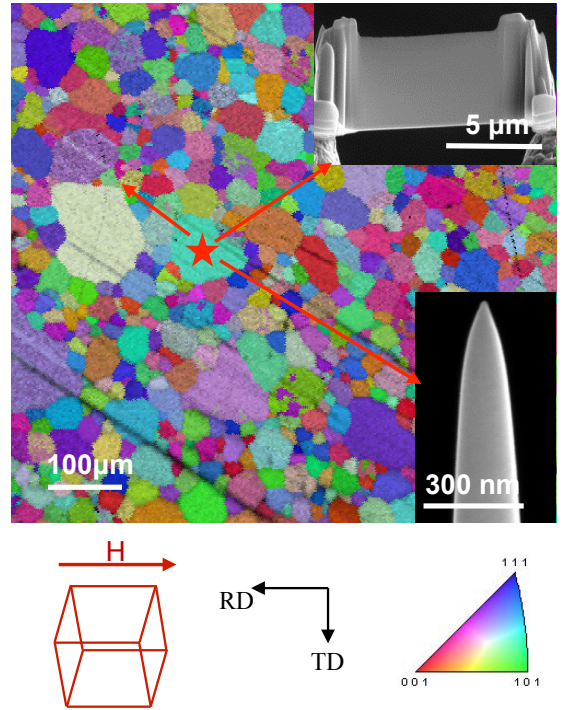


Figure 1: EBSD inverse pole figure of sample 5. Insets show a TEM (top) and APT (bottom) sample lifted from the same grain.

with their $\langle 001 \rangle$ crystal orientation parallel to the external magnetic field direction were first identified on the polished longitudinal sections (electron beam perpendicular to external field direction) using EBSD, on an Amray 1845 field emission SEM. This can exclude the effect of orientation difference between crystallographic $\langle 001 \rangle$ and external field on SD microstructure [13]. Both APT and TEM samples were then lifted-out from the same selected grain to proceed with a more detailed structural analysis, as shown in Fig. 1. An FEI Nova 200 dual-beam focused ion beam (FIB) instrument was used to perform lift-outs and annular milling of targeted grains to fabricate needle-shaped APT specimens. A wedge lift-out geometry was used to mount multiple samples on a Si microtip array to enable the fabrication of several needles from one wedge lift-out [18]. APT was performed with a local electrode atom probe (LEAP) 4000X HR manufactured by CAMECA Instruments. Samples were run in voltage mode with a base temperature of 40 K and 20% pulse fraction at a repetition rate of 200 kHz. The datasets were reconstructed and analyzed using the IVAS 3.6.12 software (CAMECA Instruments). An FEI Helios dual-beam FIB was used to perform lift-out of TEM samples with the sample surface normal parallel to the external field direction (transverse direction). An FEI probe aberration corrected Titan Themis TEM with a Super-X energy dispersive X-ray spectrometer (EDS) was used for structural characterization.

3. Experimental results

3.1. Magnetic properties

Magnetic properties of Samples 1-8 are summarized in Fig. 2. Compared with the as-solutionized sample (sam-

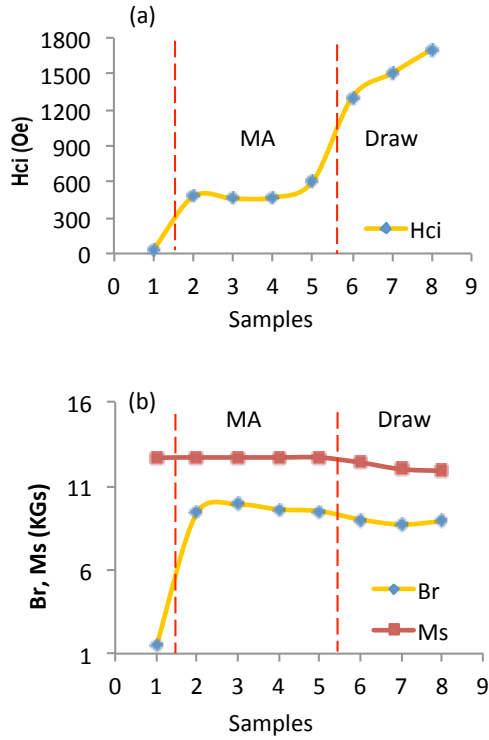


Figure 2: (a) Intrinsic coercivity (H_{ci}), (b) remanence (B_r), and saturation magnetization (M_s) of sample 1 thru 8.

ple 1), short time MA (30 s, sample 2) already results in a dramatic improvement of H_{ci} from 35 Oe to 476 Oe, and B_r from 1.5 KGs to 9.4 KGs. Increasing the MA time to 10 min further increase H_{ci} ($\sim 26\%$), but B_r plateaus between 30 s and 10 min of MA. The saturation magnetization (M_s) of sample 1 and MA samples (samples 2 to 5) is similar, indicating a similar volume fraction of the α_1 phase in those samples [6]. Drawing can triple the H_{ci} to 1707 Oe (sample 8), with the most obvious improvement occurring after the initial drawing (Sample 6); however, both M_s and B_r slightly drop after the draw.

3.2. Microstructure after solutionization

Chemical segregation has already begun after 1250 °C of solutionization, although the sample has almost no coercivity. High-angle-annular-dark-field (HAADF) scanning transmission electron microscopy (STEM) imaging was used to minimize strain contrast and differentiate phase morphology more clearly than can be achieved with traditional diffraction contrast TEM. The α_1 phase shows brighter contrast in HAADF STEM image due to the higher averaged atomic number of the elements. A mixture of ~ 5 –10 nm α_1 disks, and ~ 10 –40 nm long rods with a diameter of ~ 5 –10 nm was observed in sample 1 (Fig. 3a). The disks and rods are sometimes connected to each other. The α_1/α_2 interface is slightly blurry, which may be due to incomplete phase separation or sample thickness with respect to the 3D microstructure. Isoconcentration surfaces within the APT data of sample 1 reveals an interpenetrating nature of the α_1 and α_2 phases, as shown in Fig. 3b. The α_1 and α_2 phases are continuous with meandering boundaries within the entire analyzed volume. Both the

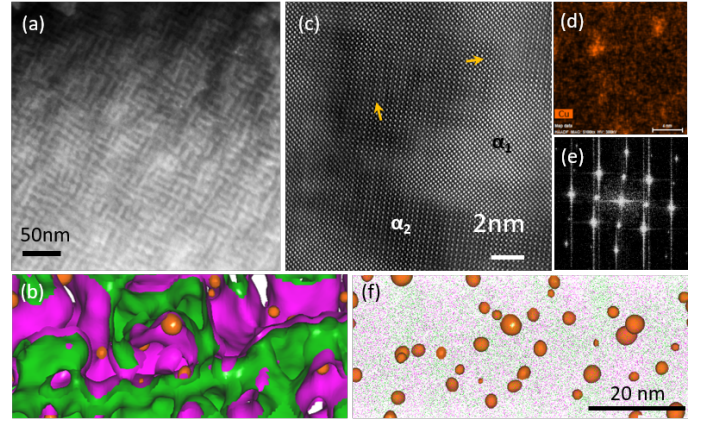


Figure 3: Sample 1 (a) HAADF STEM image showing internal SD. (b) Three-dimensional atom probe data of the as-solutionized sample (Sample 1) with isoconcentration surfaces clearly depicting the actual nanostructure of the alloy. Isoconcentration values are 7.5 at.% Ni (green), 10 at.% Cu (orange) and 30 at.% Fe (pink), which border the Ni, Cu, and Fe rich regions, respectively. (c) HRSTEM image shows a coherent lattice between α_1 , α_2 and Cu-enriched clusters. Yellow arrows indicate locations of Cu-enriched clusters. (d) and (e) are corresponding EDS Cu mapping and FFT of (c), respectively. (f) spatial distribution of Cu clusters, which are displayed by 10 at.% Cu isosurfaces. Fe and Ni atoms are also displayed.

α_1 and α_2 phases have ~ 5 –10 nm diameters. The appearance of disk and rods within the STEM images is a projected view of the α_1 phase along different crystallographic directions.

A high density of Cu-enriched clusters were detected inside α_2 , as shown in Fig. 3 b and f. The Cu-enriched clusters have an average diameter of ~ 1.2 nm and occupy $\sim 1.1\%$ of the alloy's volume. The Cu concentration at the cluster center was measured to be ~ 53.4 at.% for sample 1 by APT. High-resolution HAADF STEM image (HRSTEM, Fig. 3c) and corresponding fast-Fourier-transform (FFT) (Fig. 3e) shows coherent α_1/α_2 , α_2 /Cu interfaces. This result implies that the Cu-cluster and α_2 has the same lattice structure. Moreover, due to small size of the Cu-clusters, their positions (as indicated by arrows in Fig. 3c) in the HAADF STEM image can only be identified by overlaying the matching EDS elemental mapping (Fig. 3d).

3.3. Microstructure after magnetic field annealing

A faceted rod-shaped α_1 phase (~ 15 –20 nm) is developed during the MA process. As shown in Fig. 4a, a well-defined mosaic structure composed by a $\{110\}$ faceted α_1 phase with a ~ 10 –20 nm diameter was quickly developed in a large volume fraction of sample 2 after 30 s of MA. Some areas of sample 2 shows blurred imaging contrast, as indicated by white arrows, which implies regions with morphological differences. Increasing the MA time to 90 s (sample 3, Fig. 4c) caused a slight increase in the α_1 diameter to ~ 20 –30 nm. $\{100\}$ facets started to appear in some α_1 phases. Small α_1 particles (~ 5 nm) located between $\{100\}$ facets of two adjacent large α_1 rods were also observed, as indicated by blue arrows in Fig. 4c. Moreover, clusters of α_1 particles (~ 5 nm), as pointed out by red arrows, were formed, possibly from the white arrow regions indicated in Fig. 4a. A further MA time increase

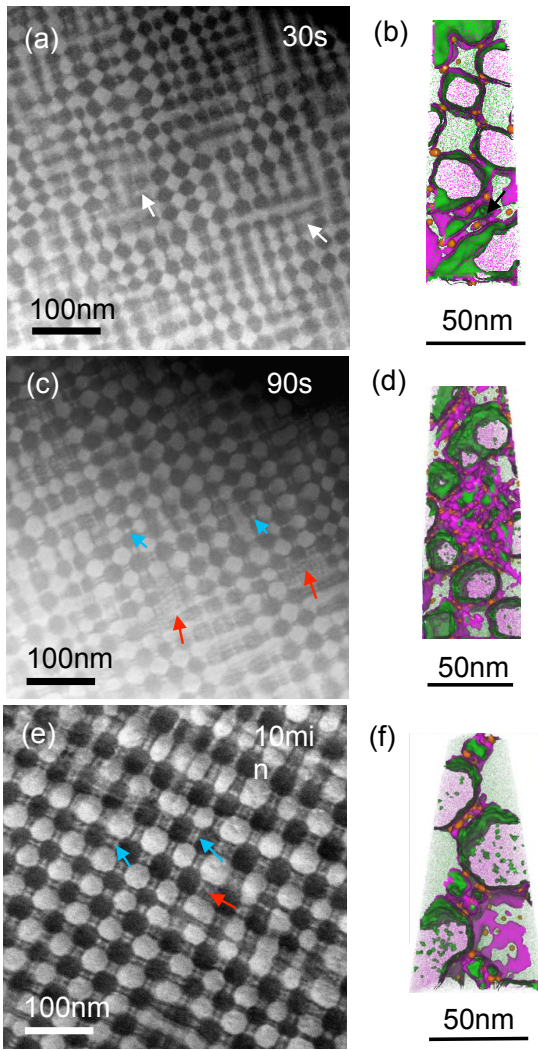


Figure 4: Nanostructures of sample 2 (a,b), sample 3 (c,d) and sample 5 (e,f) revealed by HAADF STEM images and APT. Examples of small α_1 phases between two adjacent large α_1 rods, and regions with α_1 clusters are indicated by blue and red arrows, respectively. White arrows indicate regions with a structure similar to sample 1. For clarity, the APT reconstruction only shows the Ni (green) and Fe (pink) atoms. Isoconcentration surfaces shown here are 7.5 at.% Ni (green), 10 at.% Cu (orange) and 30 at.% Fe (pink).

to 10 min (sample 5, Fig. 4e) modified the α_1 phase diameter size distribution into a bimodal distribution with large (~ 25 – 40 nm) and small (~ 5 nm) α_1 phases. Isoconcentration surfaces within the APT data clearly show α_1 phase elongation in all MA-treated samples, as demonstrated in Fig. 4b, d, and f. Regions with a morphology similar to sample 1 is also visible, as indicated by the black arrow in Fig. 4b, which may be regions indicated by the white arrow in Fig. 4a. These regions are most likely areas from the solutionization process that have not yet been modified from short time MA processes. Transformation of big isolated α_1 blocks from a parallelogram shape into an octagon shape with a cross-sectional diameter of ~ 35 nm after 10 min MA is also obvious. For all samples, the α_2 phase is continuous.

Isoconcentration surfaces within the APT data reveal that the location of Cu-enriched clusters tends to follow the edge of two adjacent $\{110\}$ facets in sample 2 (Fig. 4b).

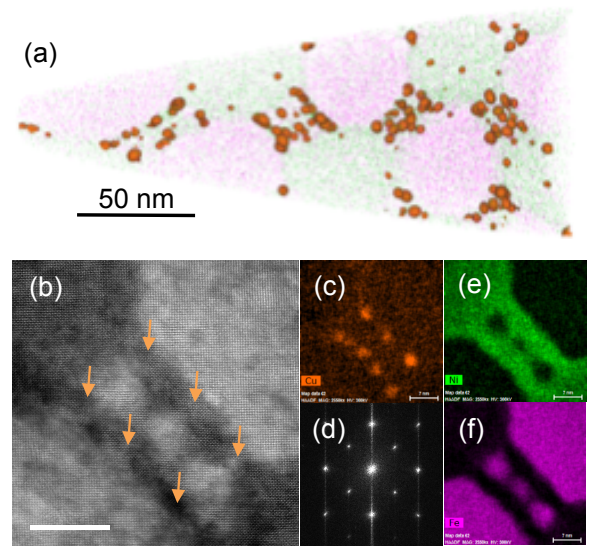


Figure 5: Sample 5 (a) APT reconstructed volumes show the distribution of Cu clusters shown by 10 at.% isoconcentration surfaces, (b) HRSTEM image and corresponding (c), (e) and (f) EDS Cu, Ni and Fe map, respectively (scale bar is 7 nm). (d) FFT of (b). Orange arrows indicate location of Cu-enriched clusters.

With increasing MA time, the region between two $\{100\}$ facets of α_1 shows a much higher Cu-enriched cluster density, as shown in Fig. 5a. This is also the area where most of the small α_1 phase is located. Figure 5b shows a HRSTEM image of sample 5. Small α_1 phases with a ~ 3 – 5 nm size are clearly visible between two $\{100\}$ facets of large α_1 rods. Locations of the Cu-clusters (indicated by orange arrows) were identified by comparing the matching EDS Cu elemental mapping (Fig. 5c). FFT analysis (Fig. 5d) shows that the Cu/ α_2 interface is coherent, which implies that the Cu-clusters still have the same lattice structure as α_2 after 10 min of MA. APT data shows no obvious change in Cu-cluster diameter (~ 1 – 1.3 nm), volume fraction (0.8–1.1 %) and composition (55–68 at.%) from sample 2 thru 5.

3.4. Microstructure after low temperature drawing

A slight increase of large α_1 rod diameters to ~ 35 – 60 nm after a 650°C low temperature draw was observed by STEM imaging and APT, as shown in Fig. 6. Small α_1 phases in between two large α_1 phases agglomerate and form smaller α_1 rods with a ~ 15 nm diameter, as indicated by blue arrows in Fig. 6a and c. Regions with α_1 clusters, as indicated by red arrows in Fig. 6a, tend to disappear after longer drawing hours (Fig. 6c). Moreover, additional α_1 phase precipitates from the α_2 phase after longer drawing hours, as shown by the pink isosurfaces within the α_2 phases in Fig. 6b and d. These α_1 clusters are slightly bigger in sample 8 than in sample 6.

A distinctive morphological change was observed for the Cu-enriched phase after drawing. A transformation from clusters to rod shapes occurs, as shown by the APT Cu elemental map in Fig. 7a. From samples 6 to 8, the Cu-rods show an average diameter of ~ 3.3 nm, which is 2–3 times larger than those found in sample 5. Moreover, the central composition of Cu tends to increase substantially from 60 at.% in sample 5 to 82 at.% in sample 6, and finally

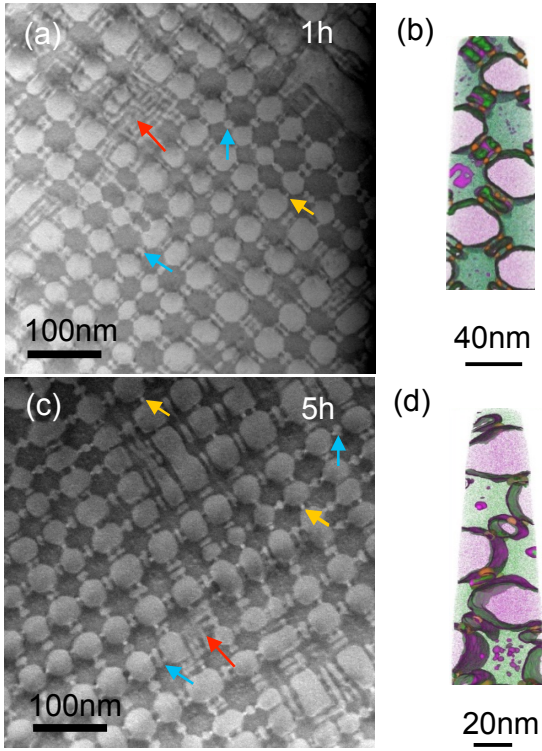


Figure 6: Nanostructures of sample 6 (a,b) and sample 8 (c,d) revealed by HAADF STEM images and APT. Examples of small α_1 rods, α_1 clusters and Cu-enriched rods are indicated by blue, red and yellow arrows respectively. For clarity, the APT reconstruction only shows the Ni (green) and Fe (pink) atoms. Isoconcentration surfaces shown here are 7.5 at.% Ni (green), 10 at.% Cu (orange) and 30 at.% Fe (pink).

to 96 at.% in sample 8. Although APT aberrations could distort the particle concentrations, with a greater distortion for smaller particles, structural differences revealed by STEM indicate a higher Cu concentration (brighter contrast) for the larger particles in sample 8, consistent with the APT results. Figure 7b shows a HAADF STEM image of sample 8, the bright contrast Cu-enriched phase is clearly visible, as confirmed by matching EDS Cu elemental mapping in Fig. 7c. The HRSTEM image shows lattice distortion in the bright Cu-enriched phase region (Fig. 7d), which is also manifested by a streaking/satellite peak in the (110) spots of the image FFT (Fig. 7e), which is further evidence that the Cu content is higher in the drawn samples.

3.5. Chemistry evolution in α_1 and α_2 phases

The α_1 and α_2 phase compositions in samples 1 thru 8 are summarized in Fig. 8. Results were extracted from cropped volumes of the APT data that were completely contained within the phases and away from the interface, so that the chemical variation caused by the interfacial profile could be excluded. The α_1 phase chemistry was relatively stable during the whole heat-treatment process, except for a slight increase in the Fe and Co content after drawing. More obvious chemistry changes were detected in the α_2 phase. After the first 30s of MA, there was an increase of Co and Ti content, and a decrease of Al content, while the chemical composition tends to be stable during

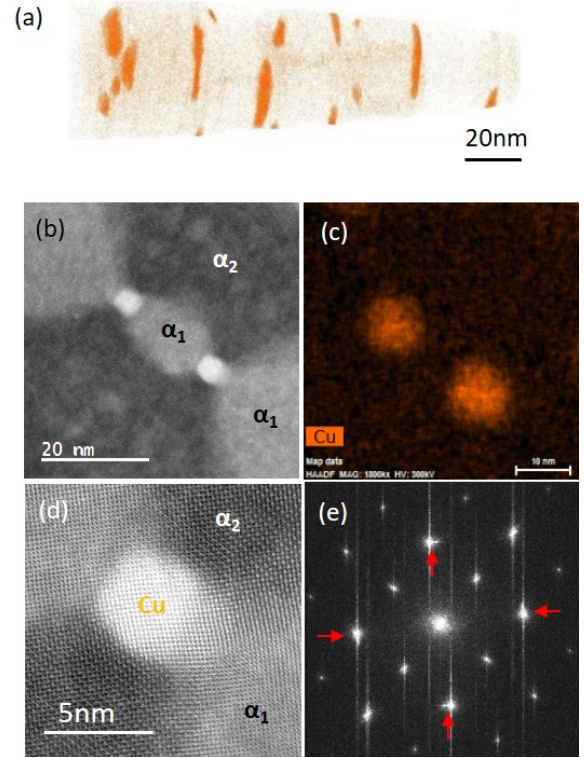


Figure 7: Sample 7 (a) Cu atom map in the reconstructed APT volume, (b) HAADF STEM image and corresponding (c) EDS Cu mapping (scale bar is 10 nm). (d) HRSTEM image shows lattice distortion in the Cu-enriched phase. (e) FFT of (d) with red arrows indicating splitting of (110) diffraction spots.

the following MA processes. Drawing at 650 °C gradually increased the Al and Ni concentration, while that of Co and Fe decreased. The Ti concentration plateaued during the MA and drawing step. This indicates that the diffusion speed of all elements is fast enough at 840 °C to approach its thermodynamically stable concentration within 30 s, however, there is an obvious diffusion speed decrease at 650 °C, and therefore, it takes a much longer time to reach the equilibrium concentration.

4. Discussion

The APT combined with detailed TEM and magnetization measurements provide a clear picture of relationships between the phase evolution and magnetic properties. Observation of phase separation in sample 1 indicates that oil quenching cannot provide a fast enough quench to bypass initiation of the SD. After only 30 s of MA, the optimal coercivity imparted from this step is observed, even though the APT and TEM shows further morphological changes up to 10 min of MA. The small changes in chemistry from sample 2 to 5 implies that the chemical diffusion is rapid and the observed gradual morphology change is more likely to be driven by minimization of interfacial and magnetic energy. After MA, particles are not only elongated, but also become less interconnected to each other, which helps increase H_{ci} .

The 650 °C draw has a remarkable effect on both H_{ci} and refinement of the chemistry between the α_1 and α_2

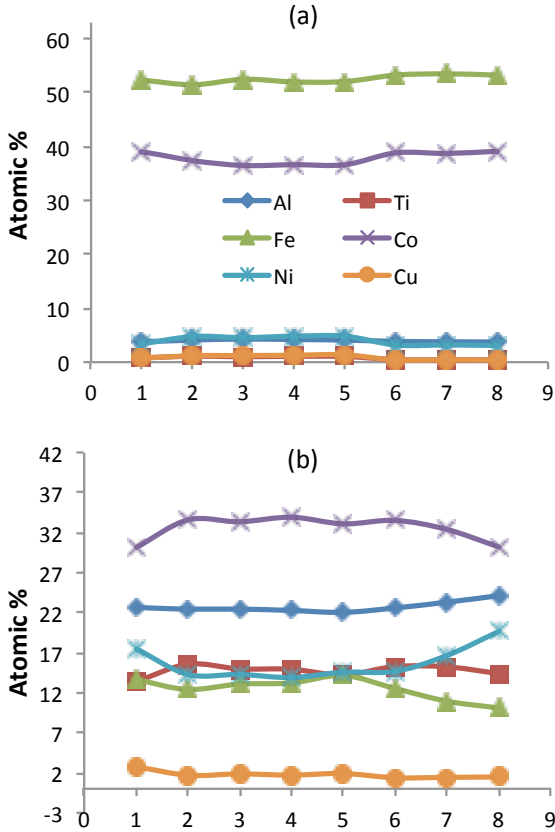


Figure 8: The elemental composition of α_1 (a) and α_2 phases (b) measured by atom probe tomography from sample 1 thru 8.

phases. The conventional explanation is that drawing further increases the chemical separation of the two phases [19]. However, our results suggest that the draw effect on H_{ci} enhancement likely involves several mechanisms, including chemistry, ordering, as well as subtle structural features, such as evolution of the Cu-enriched phase. For the α_1 phase, the Fe and Co concentration slightly increases after the first draw step (comparing sample 5 and 6), then it is nearly constant. On the other hand, in the α_2 phase, Fe and Co contents continue to decrease with increasing draw time, which is likely due to the coarsening/growth α_1 in α_2 of precipitates. Overall, the chemical variation is small and may not change the magnetization of the α_2 phase significantly. On the other hand, site ordering in the α_2 phase may play an important role. Our previous study showed that formation energy is lower and T_C decreases with increasing α_2 site ordering (from BCC to DO₃ and L2₁) [6]. Thus, draw annealing may promote site ordering in the α_2 region, possibly due to a decreases in the Fe and Co content in the α_2 phase. Considering that T_C of α_2 is near room temperature, both chemistry changes and site ordering decrease magnetization of the α_2 phase at room temperature, which increases H_{ci} .

The most dramatic change is in the growth of the Cu-enriched regions. Transformation of small Cu-enriched clusters into larger and longer Cu-enrich rods may be driven by minimization of interfacial energy as the center of the clusters has higher and higher Cu concentration. Similar elongated precipitates along elastic soft [100] direction has

been reported in Cu₂at.%Co system [?]. These elongated large Cu-rods may provide better pinning for magnetic domain wall movement. The Cu-enriched phase not only becomes bigger and longer but also less magnetic, which can further separate α_1 rods. The Cu lattice shearing from the *bcc* structure may be because the *fcc* structure of Cu is thermodynamically more stable. Moreover, since some branching types may be very detrimental to H_{ci} , a larger Cu cluster can isolate two originally connected α_1 rods and increases H_{ci} [20]. Finally, formation of small α_1 rods or even chains of spheres, along with the previously reported formation of Ni-rich (α_3) separation phase at the α_1/α_2 interface can also help to increase H_{ci} [21].

5. Conclusions

Coercivity enhancement is a complex interplay between the intrinsic properties of the alnico alloy and its nanostructure. With MA, the kinetics of the SD is rapid and the near optimum geometric spacing is quickly reached due to higher annealing temperature. MA sets the template for the spinodal and locks in remanence, while the draw process is responsible for the finer microstructural and chemical tuning, which controls the coercivity. The profound effect of draw on improving H_{ci} is likely due to a combination of several mechanisms, including chemical, site ordering, and subtle microstructural variations. The draw process does not introduce dramatic microstructural changes of α_1 and α_2 phases, but does affect the size, shape, and distribution of the intervening Cu-rich phase forming in-between these phases. This new understanding provides possible directions for further property enhancement of alnico.

Acknowledgment

Research was supported by U.S. DOE, Office of Energy Efficiency and Renewable Energy (EERE), under its Vehicle Technologies Office, Electric Drive Technology Program, through the Ames Laboratory, Iowa State University under contract DE-AC02-07CH11358. APT rwas conducted at ORNL's Center for Nanophase Materials Sciences (CNMS), which is a DOE Office of Science User Facility.

References

References

- [1] R. McCurrie, Chapter 3 the structure and properties of alnico permanent magnet alloys, volume 3 of *Handbook of Ferromagnetic Materials*, Elsevier, 1982, pp. 107–188.
- [2] T. Watanabe, S. Tsurekawa, X. Zhao, L. Zuo, Grain boundary engineering by magnetic field application, *Scripta Materialia* 54 (2006) 969–975.
- [3] T. Watanabe, S. Tsurekawa, X. Zhao, L. Zuo, C. Esling, A new challenge: grain boundary engineering for advanced materials by magnetic field application, *Journal of Materials Science* 41 (2006) 7747–7759.
- [4] J. W. Cahn, Magnetic aging of spinodal alloys, *Journal of Applied Physics* 34 (1963) 3581–3586.

- [5] M. Kramer, R. McCallum, I. Anderson, S. Constantinides, Prospects for non-rare earth permanent magnets for traction motors and generators, *JOM Journal of the Minerals, Metals and Materials Society* 64 (2012) 752–763.
- [6] L. Zhou, M. Miller, P. Lu, L. Ke, R. Skomski, H. Dillon, Q. Xing, A. Palasyuk, M. McCartney, D. Smith, S. Constantinides, R. McCallum, I. Anderson, V. Antropov, M. Kramer, Architecture and magnetism of alnico, *Acta Materialia* 74 (2014) 224–233.
- [7] R. McCallum, L. Lewis, R. Skomski, M. Kramer, I. Anderson, Practical aspects of modern and future permanent magnets, *Annual Review of Materials Research* 44 (2014) 451–477.
- [8] M. Stanek, L. Wierzbicki, M. Leonowicz, Investigations of thermo-magnetic treatment of alnico 8 alloy, *Archives of Metallurgy and Materials Vol. 55* (2010) 571–577.
- [9] V. Sergeev, T. Bulygina, Magnetic properties of alnico 5 and alnico 8 phases at the sequential stages of heat treatment in a field, *Magnetics, IEEE Transactions on* 6 (1970) 194–198.
- [10] M. Takeuchi, Y. Iwama, Effects of titanium upon magnetic anisotropy and coercivity in alnico magnet alloys, *Transactions of the Japan Institute of Metals* 17 (1976) 489–496.
- [11] Y. Iwama, M. Takeuchi, Spinodal decomposition in alnico 8 magnet alloy, *Transactions of the Japan Institute of Metals* 15 (1974) 371–377.
- [12] Y. Iwama, M. Inagaki, T. Miyamoto, Effects of titanium in alnico 8-type magnet alloys, *Transactions of the Japan Institute of Metals* 11 (1970) 268–274.
- [13] L. Zhou, M. K. Miller, H. Dillon, A. Palasyuk, S. Constantinides, R. W. McCallum, I. E. Anderson, M. J. Kramer, Role of the applied magnetic field on the microstructural evolution in alnico 8 alloys, *Metallurgical and Materials Transactions E* 1 (2014) 27–35.
- [14] L. Zhou, W. Tang, L. Ke, W. Guo, J. D. Poplawsky, I. E. Anderson, M. J. Kramer, Microstructural and magnetic property evolution with different heat-treatment conditions in an alnico alloy, *Acta Materialia* 133 (2017) 73 – 80.
- [15] W. Tang, L. Zhou, A. G. Kassen, A. Palasyuk, E. M. White, K. W. Dennis, M. J. Kramer, R. W. McCallum, I. E. Anderson, New alnico magnets fabricated from pre-alloyed gas-atomized powder through diverse consolidation techniques, *IEEE Transactions on Magnetics* 51 (2015) 1–3.
- [16] M. K. Miller, K. F. Russell, Performance of a local electrode atom probe, *Surface and Interface Analysis* 39 (2007) 262–267.
- [17] D. B. Williams, C. B. Carter, *The Transmission Electron Microscope*, Springer US, Boston, MA, 1996.
- [18] K. Thompson, D. Lawrence, D. Larson, J. Olson, T. Kelly, B. Gorman, In situ site-specific specimen preparation for atom probe tomography, *Ultramicroscopy* 107 (2007) 131–139.
- [19] R. McCurrie, S. Jackson, Rotational hysteresis and magnetization curling of elongated single-domain particles in alnico permanent magnets, *IEEE Transactions on Magnetics* 16 (1980) 1310–1319.
- [20] L. Ke, R. Skomski, T. D. Hoffmann, L. Zhou, W. Tang, D. D. Johnson, M. J. Kramer, I. E. Anderson, C.-Z. Wang, Simulation of alnico coercivity, *Applied Physics Letters* 111 (2017) 022403.
- [21] M. C. Nguyen, L. Zhou, W. Tang, M. J. Kramer, I. E. Anderson, C.-Z. Wang, K.-M. Ho, Cluster-expansion model for complex quinary alloys: Application to alnico permanent magnets, *Phys. Rev. Applied* 8 (2017) 054016.